AIP | Review of Scientific Instruments

A high time resolution x-ray diagnostic on the Madison Symmetric Torus

Ami M. DuBois, John David Lee, and Abdulgadar F. Almagri

Citation: Review of Scientific Instruments **86**, 073512 (2015); doi: 10.1063/1.4927454
View online: http://dx.doi.org/10.1063/1.4927454
View Table of Contents: http://scitation.aip.org/content/aip/journal/rsi/86/7?ver=pdfcov
Published by the AIP Publishing

A high time resolution x-ray diagnostic on the Madison Symmetric Torus

Ami M. DuBois, John David Lee, and Abdulgadar F. Almagri
Department of Physics, University of Wisconsin–Madison, Madison, Wisconsin 53706, USA

(Received 11 May 2015; accepted 14 July 2015; published online 28 July 2015)

A new high time resolution x-ray detector has been installed on the Madison Symmetric Torus (MST) to make measurements around sawtooth events. The detector system is comprised of a silicon avalanche photodiode, a 20 ns Gaussian shaping amplifier, and a 500 MHz digitizer with 14-bit sampling resolution. The fast shaping time diminishes the need to restrict the amount of x-ray flux reaching the detector, limiting the system dead-time. With a much higher time resolution than systems currently in use in high temperature plasma physics experiments, this new detector has the versatility to be used in a variety of discharges with varying flux and the ability to study dynamics on both slow and fast time scales. This paper discusses the new fast x-ray detector recently installed on MST and the improved time resolution capabilities compared to the existing soft and hard x-ray diagnostics. In addition to the detector hardware, improvements to the detector calibration and x-ray pulse identification software, such as additional fitting parameters and a more sophisticated fitting routine are discussed. Finally, initial data taken in both high confinement and standard reversed-field pinch plasma discharges are compared. © *2015 AIP Publishing LLC.* [http://dx.doi.org/10.1063/1.4927454]

I. INTRODUCTION

X-ray detectors have become an increasingly useful diagnostic for both laser produced plasma[1,2] and high temperature plasma[3–10] experiments. Laser produced plasma experiments require time resolution on the pico-second time scale, whereas high temperature plasma physics experiments generally require good energy resolution for line radiation studies.[10,11] However, more recent detector systems[5,6,9,11,12] have exchanged energy resolution for improved time resolution to study temporal dynamics of fast electrons. These improved time resolution x-ray diagnostics utilize solid state detectors with pulse shaping times of approximately 1 μs, energy resolutions of hundreds of eV, and digitization rates of 2–10 MHz. On the Madison Symmetric Torus[13] (MST) reversed-field pinch (RFP), current x-ray diagnostics consist of a radial array of Si photodiode Amptek detectors and CdZnTe eV Products detectors,[9,14] and a new Si avalanche photodiode fast x-ray detector, which is the focus of this paper. The Amptek detectors have an energy resolution of 0.45 keV with a shaping time of 0.24 μs, and the eV Products detectors have an energy resolution of 2 keV with a shaping time of 1.2 μs.[9]

Previous experiments on MST using the existing radial array of soft x-ray (SXR) and hard x-ray (HXR) detectors have indicated the need for high time resolution measurements. These experiments found the particle transport is greatly reduced in high confinement RFP plasma discharges, with diffusion rates of electrons of approximately 5 m^2/s.[15,16] Experimental focus has recently shifted toward studying electron energization at sawtooth events in standard RFP plasma discharges, where the diffusion rates are approximately 25 m^2/s.[15] During standard RFP plasma discharges, magnetic islands begin to overlap and create stochastic magnetic fields that facilitate particle transport away from the plasma core.[17] In particular, electrons, which are tightly bound to magnetic fields, will diffuse radially outward to the vacuum vessel wall at a rate that is proportional to the parallel velocity, so that the most energetic electrons are lost from the plasma core much faster than the thermal population of electrons.[18] Due to the rapid thermal transport at sawtooth events, it is hypothesized that the generation and loss of energetic electrons may occur on a much faster time scale than the current detectors available on MST are capable of measuring. This is supported by experiments by Scime *et al.*,[19] Magee *et al.*,[20] and Eilerman *et al.*[21] where the ion population was found to be energized at sawtooth events, but Thomson scattering measurements showed the electron temperature decreased. Therefore, high time resolution measurements are required to uncover evidence of possible electron energization.

A Si Avalanche Photodiode[22,23] (APD) detector with an optimal energy range of 2–30 keV and an energy resolution of 0.974 keV at 5.9 keV has been installed on MST. The Si-APD detector is most commonly used in nuclear resonant scattering experiments using synchrotron radiation x-rays, which requires high time resolution because x-ray pulse separation can be as little as 2–3 ns.[22,24] The detector, which has a 20 ns shaping time and a digitization rate of 500 MHz, has a much higher time resolution than current detectors used in high temperature plasma experiments. This allows for the measurement of significant x-ray flux in time windows as small as 10 μs. Section II provides a description of the Fast X-Ray (FXR) detector, the calibration process, and the improved signal processing technique, and Section III reports on the initial data measured by the detector.

II. DIAGNOSTIC DESCRIPTION

A. Fast X-ray detector

The FXR detector is a high time resolution soft x-ray spectrometer that measures electron energization via emitted bremsstrahlung and has recently been installed on MST. The

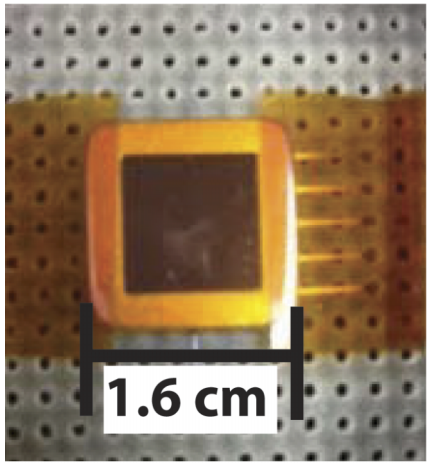

FIG. 1. The Si avalanche photodiode crystal with a 10×10 mm^2 active area used in the fast x-ray detector on MST.

detector, shown in Fig. 1, consists of a PerkinElmer Inc., Si-APD (type C30703F) with a 10 mm $\times$ 10 mm active area. A high voltage power supply is used to apply a bias of +430 V to the APD. The APD output signal is proportional to the energy of the incident photon and is input to a Gaussian amplifier with a shaping time of 20 ns. The shaping amplifier increases the magnitude of the signal while reducing the noise level. The full width-half maximum (FWHM) of each Gaussian pulse is approximately equal to 20 ns, allowing for high time resolution measurements.

The detector crystal and the shaping amplifier are placed in close proximity in order to reduce the noise pickup in the circuitry. Using a ZT410PXI-21 ZTec digitizer with a 14-bit sampling resolution, the amplified signal is digitized at a rate of 500 MHz, which allows 16 million samples to be taken over a 32 ms window. An example of the digitized signal over a 1 ms time window is shown in Fig. 2. Each spike represents an individual photon pulse where the peak voltage is directly proportional to the energy of the incident photon.

The detector is located on an inboard port of MST with a chord view through the core of MST. The detector has the versatility to be quickly moved to ports for measurements

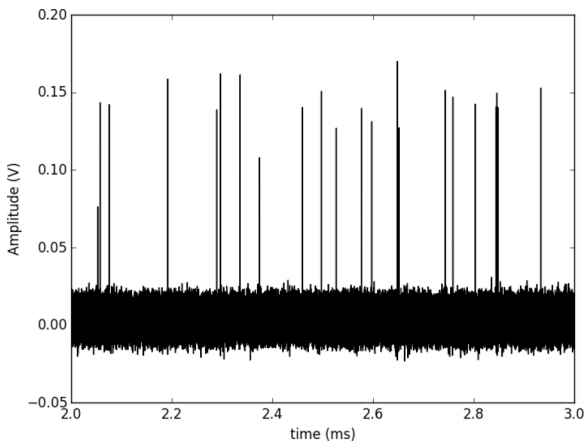

FIG. 2. Photon pulses from the Fe55 calibration source measured by the FXR detector over a time window of 1 ms.

through chords viewing different impact parameters. Each x-ray detector port is fitted with a 150 μm beryllium (Be) window that separates the detector from vacuum and filters out photons with energies less than 2 keV. Apertures with diameters ranging from 0.5 mm to 6.4 mm are separated by 3 cm of air and serve to collimate and focus the detector view if necessary.

The fast shaping time of the FXR detector system greatly reduces the chances of pulse pile-up from occurring, thus limiting the system dead-time to nanosecond time scales.[22] Pulse pile-up and system resets caused by integrated x-ray flux in the existing slower SXR and HXR detector systems caused an unacceptable system dead-time of approximately 1 ms, and consequently, the flux reaching the detectors had to be highly restricted via highly collimated views. The poor counting statistics that resulted from restricting the x-ray flux had to be compensated for by taking data over a large number of discharges and averaging them together. Because the FXR detector system is so much faster, the need to collimate the detector view and restrict x-ray flux is not as crucial, giving the FXR detector system the versatility to be used in conditions with a wide range of varying x-ray flux.

B. Calibration

A radioactive iron source (Fe55) with an energy of 5.889 keV is used to calibrate the FXR detector system and derive a characteristic pulse. The characteristic pulse is used to determine if the x-ray signal is a photon pulse or noise. This technique is used opposed to a Gaussian model because the Gaussian fits led to an increase in the number of events where noise was accepted as a photon pulse. The characteristic pulse is fit to all signals in the calibration dataset, and if the signal is determined to be a photon pulse, the pulse amplitudes are recorded and a spectrum of amplitudes is calculated. This spectrum is used to calculate a scaling factor to convert the output voltage to x-ray energy. A spline fit is also applied to each photon pulse and the FWHM is calculated, which is used in conjunction with a goodness of fit parameter to help determine if a signal measured in a plasma discharge is noise or a photon pulse. This improved calibration process yields more accurate and reliable fits to photon pulses taken in plasma discharges.

The characteristic pulse is calculated from the Fe55 source data by selecting pulses that are above a threshold of 0.05 V, as is shown in Fig. 2, and are separated by at least 3 μs in time from other pulses in order to ensure that the photon pulse baseline returns to zero. Each pulse that meets these criteria is normalized by its maximum amplitude. The characteristic pulse is derived from the average of normalized pulses. The calibration data are taken in a low noise environment to keep the noise level at a minimum and prevent noise-like pulses from altering the calculated characteristic pulse.

Once a clean characteristic pulse is created, all Fe55 pulses in the energy calibration data with amplitudes greater than 0.05 V are selected and used to calculate an energy spectrum of the Fe55 line. These pulses do not have to be separated by any amount of time from other pulses. The characteristic pulse is fit to each of the detected pulses using pulse height analysis software developed in Python. The characteristic

pulse shape can be described by the linear model,

$$f_i = Ap_i + s, \tag{1}$$

where A is the pulse amplitude, p_i is the ith element in the normalized characteristic pulse shape array, and s is the offset. The offset, which can be positive or negative, is due to noise in the signal or from lack of baseline restoration before the next pulse is measured. Assuming the length of all arrays is N, fitting the characteristic pulse model array (f_i) to the detected photon pulse (d_i) requires minimizing the sum-of-square error (SSE),

$$\begin{aligned} SSE &= \sum_i^N (f_i - d_i)^2 \\ &= \left(A^2P_2 + Ns^2 + D_2 + 2AsP_1 - 2AQ - 2sD_1\right), \end{aligned} \tag{2}$$

where,

$$\begin{aligned} Ns^2 &= \sum_i^N s^2, \\ P_1 &\equiv \sum_i^N p_i, \\ P_2 &\equiv \sum_i^N p_i^2, \\ D_1 &\equiv \sum_i^N d_i, \\ D_2 &\equiv \sum_i^N d_i^2, \\ Q &\equiv \sum_i^N d_i p_i. \end{aligned} \tag{3}$$

The best-fit amplitude and offset are computed by setting the partial derivative of SSE to zero with respect to each of the fitting parameters such that,

$$\begin{aligned} &\frac{\partial}{\partial A}\left(A^2P_2 + Ns^2 + D_2 + 2AsP_1 - 2AQ - 2sD_1\right) \\ &\quad = AP_2 + sP_1 - Q = 0, \end{aligned} \tag{4a}$$

$$\begin{aligned} &\frac{\partial}{\partial s}\left(A^2P_2 + Ns^2 + D_2 + 2AsP_1 - 2AQ - 2sD_1\right) \\ &\quad = Ns + AP_1 - D_1 = 0. \end{aligned} \tag{4b}$$

Solving Eq. (4a) for A yields the best-fit amplitude between the characteristic pulse model and the raw photon pulse,

$$A = \left(Q - P_1 s\right)/P_2. \tag{5}$$

Substituting Eq. (5) into Eq. (4b) and solving for s yields the pulse offset relative to 0,

$$s = \left(D_1P_2 - P_1Q\right)/\left(NP_2 - P_1^2\right). \tag{6}$$

Fig. 3 shows an example of the characteristic pulse model (red) fit to a raw Fe55 photon pulse (black) with a calculated offset of −9.94 mV and a best-fit amplitude of 0.136 V.

The best-fit amplitudes for each photon pulse detected in the calibration data are binned together to plot a spectrum of amplitudes. To calculate a scaling factor to convert volts to energy, a Gaussian curve is fit to the spectrum. The peak number of counts corresponds to a best-fit amplitude of 0.138 V and is proportional to the energy of the Fe55 source. This yields a conversion factor of 42.64 V/keV. The energy spectrum for Fe55 measured by the FXR detector is shown in Fig. 4, with the peak number of counts located at an energy of 5.889 keV. The FWHM of the energy distribution yields an energy resolution of 0.974 keV for the FXR detector.

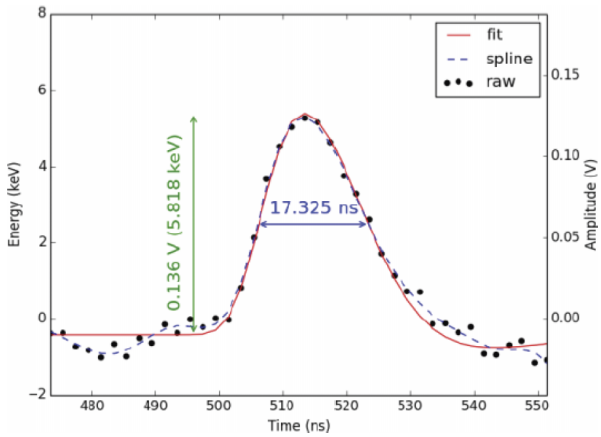

FIG. 3. A single Fe55 photon pulse (black) measured by the FXR detector with the characteristic pulse fit (red) and the spline fit (dashed, blue). The best-fit amplitude is 0.136 V (5.818 keV) with an R^2 value of 0.981 and a full width-half maximum, as calculated from the spline fit, of 17.325 ns.

Each recorded photon pulse from the plasma is distinguished from noise in experimental data using the FWHM of the photon pulses and the coefficient of determination, R^2, which quantifies a goodness of fit between the characteristic model and the raw data. In order to calculate appropriate limits to be used for experimental data, the FWHM and R^2 are calculated for all of the Fe55 photon pulses in the calibration data. The SSE in Eq. (2) and the total sum-of-squares (SST) in Eq. (7a) are used to calculate R^2 (Eq. (7b)),

$$SST = \sum_i \left(d_i - \bar{d}\right)^2, \tag{7a}$$

$$R^2 = 1 - \left(SSE/SST\right), \tag{7b}$$

where $\bar{d}$ is the mean of the raw photon pulse. The FWHM of each photon pulse is calculated from a spline-fit. The R^2 value between the pulse and fit shown in Fig. 3 is 0.981 with a FWHM of 17.325 ns, with the spline fit to the raw data shown in blue (dashed). The best-fit amplitude converted to

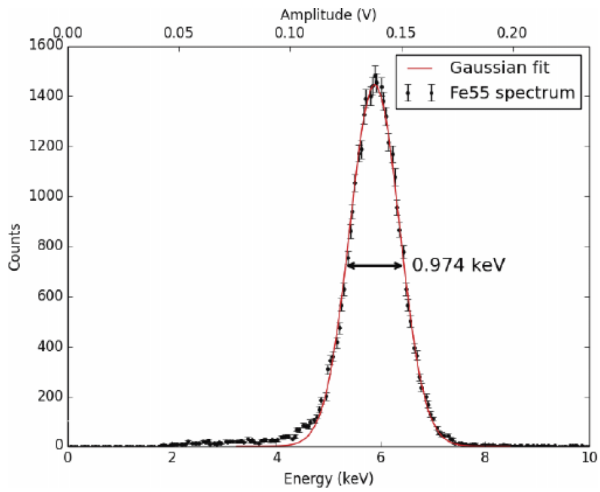

FIG. 4. The Fe55 energy spectrum (black) measured by the FXR detector and the Gaussian fit (red). The full width-half maximum (0.974 keV) is calculated from the Gaussian fit and is equal to the energy resolution of the detector.

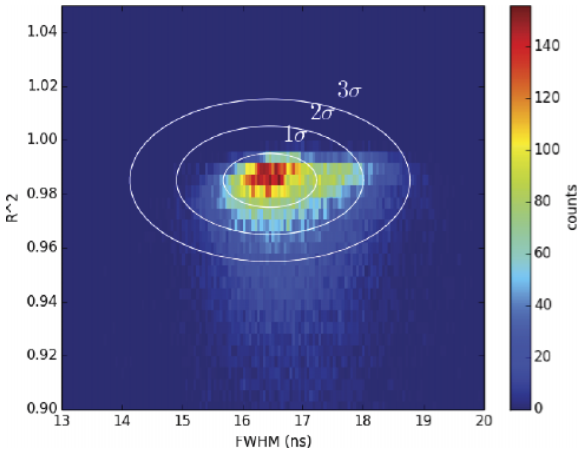

FIG. 5. A 2D histogram of the calculated R^2 and FWHM (pulse shaping time) for all Fe55 photon pulses detected in the calibration data, where the color indicates the number of counts. The white ellipses represent the standard deviation of the distributions. The central R^2 value is 0.985 with a standard deviation of ±0.01. The central FWHM is 16.456 ns with a standard deviation of ±0.77 ns.

energy using the conversion factor is 5.818 keV. Fig. 5 shows a histogram of the calculated R^2 as a function of the FWHM for all detected pulses in the Fe55 calibration data. The color scale indicates the number of counts, with the highest number of counts shown in red, and no counts shown in dark blue. The peak of the histogram is centered around $R^2 = 0.985 \pm 0.01$ and a FWHM of 16.456 ± 0.77 ns. The horizontal/vertical extent of the contours shown in white indicates the multiple levels of the standard deviation ($n\sigma$ where n = 1, 2, 3) of the FWHM/R^2.

C. Data processing and spectra calculations

Using Python, software was developed to perform pulse height analysis on experimental data. The raw data are converted from volts to energy using the scaling factor described above. Any photon pulse above a noise floor threshold of 2 keV is identified by the software and is fit with the characteristic pulse using the same method described in Sec. II B. If the R^2 value between the raw photon pulse and the characteristic pulse fit is greater than 0.9 and the FWHM falls within the range of 16.456 ns ± 2σ where σ = 0.77 ns, then the signal is considered to be a real photon pulse and the data are recorded and stored for later use.

In previous versions of the pulse height analysis,[9] a Gaussian curve of fixed width was fit to each pulse instead of a characteristic pulse derived from a known x-ray source during calibration. This Gaussian technique led to an increase in the number of events where noise was accepted as a photon pulse. The additions of the characteristic pulse fit and calculation of the pulse FWHM have been major improvements, yielding more accurate and reliable fits to raw photon pulses.

To calculate an energy spectrum, a series of similar discharges is taken, and all pulses are counted and separated into a range of energy bins for the full ensemble of shots. For the FXR detector, the smallest time window with sufficient statistics is approximately 10 μs. To calculate the total x-ray flux collected by the detector as a function of time and energy, the spectrum is divided by the collection time and the energy bin width. The resulting spectrum is then corrected by dividing the detector efficiency, which is dependent on the probability of transmission through a number of materials and the probability of a photon interacting with the silicon detector.

III. INITIAL MEASUREMENTS

Initial FXR data have been measured in three types of discharges in MST. In Fig. 6(a), FXR data are plotted as a function of time during the flattop period of a 500 kA standard RFP plasma discharge, which has a fast, dynamic behavior that is reflected in the FXR data. In Fig. 6(b), the m = 1, n = 6 tearing mode amplitude (black) and magnetic energy (red) are shown for the same time period. Both the n = 6 amplitude and the magnetic energy increase between sawtooth crashes, a period delineated by the blue dashed lines. During this time, the high energy x-ray flux increases, but the maximum photon energy remains less than 20 keV. Around the sawtooth crash, photons up to 30 keV are observed by the FXR detector, but disappear in less than 50 μs. After the crash, the total x-ray flux is significantly decreased, with energies less than 20 keV. This indicates that the confinement time in standard plasma discharges is very short due to a stochastic core developing from overlapping tearing mode islands. This is consistent with previous x-ray spectroscopy data taken in

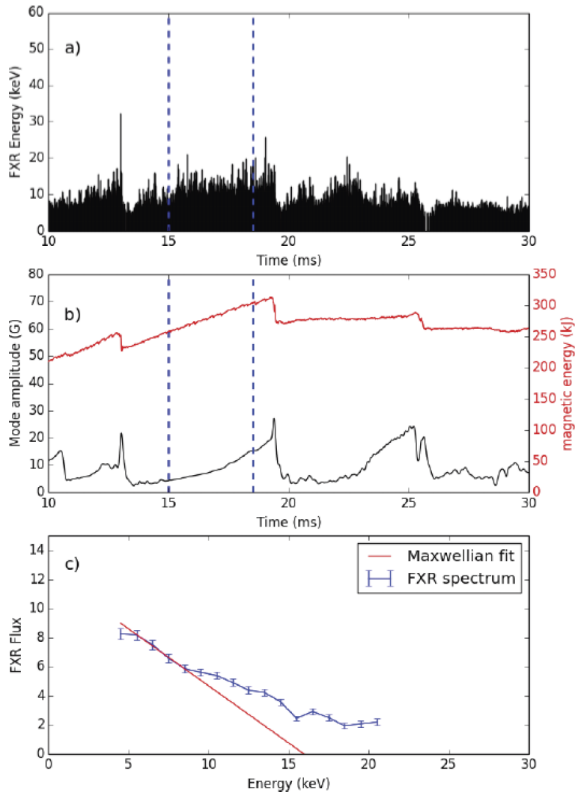

FIG. 6. Data taken in a 500 kA standard plasma discharge in MST. (a) Photon pulses measured by the FXR detector during the flattop period between 10 and 30 ms. (b) The m = 1, n = 6 tearing mode amplitude (black) and the magnetic energy (red). A sudden drop in the magnetic energy indicates a sawtooth event. (c) The energy spectrum (blue) is calculated for the times between the blue dashed lines in (a) and (b) with a Maxwellian curve fit to the spectrum (red).

standard plasmas.[15] Fig. 6(c) shows the FXR spectrum (blue) calculated between sawteeth from 15 ms to 19 ms (dashed lines, blue). A Maxwellian curve (red) is fit to the low energy part of the spectrum (4 to 8.5 keV) to expose the difference between the calculated Maxwellian and the measured spectrum above 8.5 keV and show the presence of an energetic tail between sawteeth. The time resolution of the FXR detector will allow the measurements of energy spectra around sawtooth crashes to be made with far fewer discharges and on time scales of 10 μs, much improved compared to the existing HXR detectors, which cannot make measurements of resolved spectra on time scales this low due to the slower time resolutions of 1.2 μs.

FXR measurements in standard plasmas are compared to other MST discharges where the stochasticity is greatly reduced. FXR data taken in a 500 kA, non-reversed, quasi-single helicity (QSH)[25] discharge is shown in Fig. 7(a). In the QSH discharge, a single magnetic island spontaneously forms in the plasma at the m = 1, n = 5 rational surface while all other tearing mode amplitudes are reduced,[26] as shown in Fig. 7(b). Fig. 7(a) shows that while the n = 5 mode amplitude is growing, the high energy x-ray flux is greatly increased compared to the standard plasma discharge. This indicates that fast electrons are generated within the island. The fast electrons remain confined in the plasma for several milliseconds, longer than the confinement time in standard plasmas. When the n = 5 mode amplitude saturates, the high energy x-ray flux disappears, indicating that the fast electrons may be lost from the plasma core. Fig. 7(c) shows the FXR spectrum (blue) calculated during the growth phase of the n = 5 mode from 19 ms to 24 ms, as indicated by the blue, dashed lines. The measured spectrum shows an energetic tail develops when the n = 5 amplitude is growing. A Maxwellian curve (red) is fit to the spectrum for energies between 4 keV and 8.5 keV to expose the difference between the calculated Maxwellian and the measured spectrum during the growth phase of QSH. These initial results in QSH plasmas are consistent with those measured using HXR detectors in previous experiments by Clayton *et al.*[16] New experiments are being performed to study fast electron generation during QSH discharges in MST. In these new experiments, the fast shaping time of the FXR detector is vital for comparing the effect of changes in the density, the locking time of the mode, and the locking position of the mode on the generation and suppression of fast electrons.

In MST discharges with pulsed parallel current drive (PPCD),[27,28] the current density profile is inductively modified to stabilize and reduce tearing mode amplitudes. FXR data measured during a 500 kA PPCD discharge are shown in Fig. 8(a). During the PPCD period, there is a reduction in all

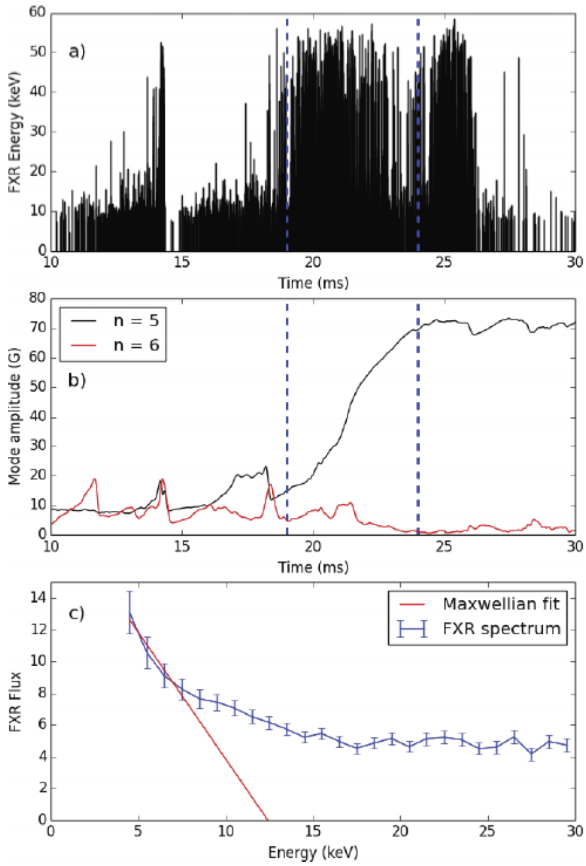

FIG. 7. Data taken in a 500 kA QSH discharge in MST. (a) Photon pulses measured by the FXR detector between 10 and 30 ms. (b) Amplitudes of the m = 1, n = 5 tearing mode (black) and the m = 1, n = 6 tearing mode (red). (c) The energy spectrum (blue) is calculated for the times between the blue dashed lines in (a) and (b) during the growth of the n = 5 tearing mode with a Maxwellian curve fit to the spectrum (red).

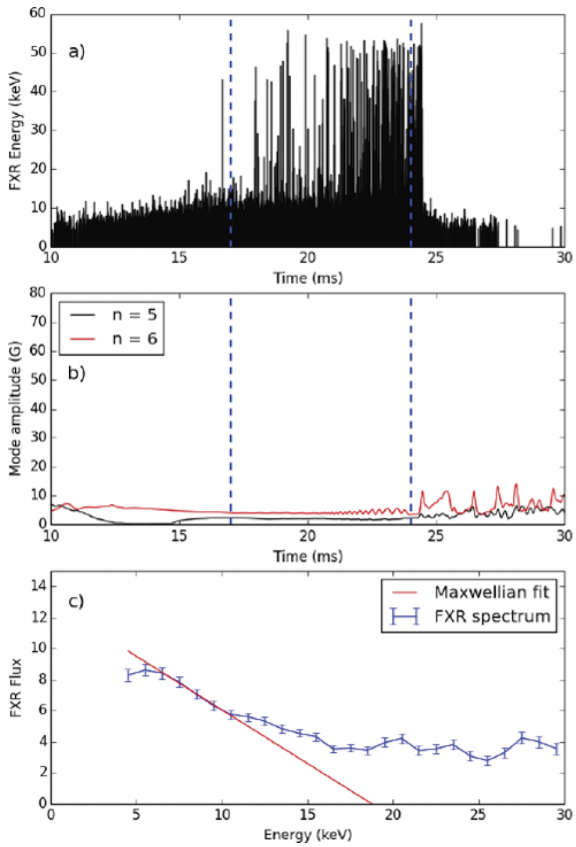

FIG. 8. Data taken in a 500 kA PPCD discharge. (a) Photon pulses measured by the FXR detector between 10 and 30 ms. (b) The m = 1, n = 5 tearing mode amplitude (black) and the m = 1, n = 6 tearing mode amplitude (red). (c) The energy spectrum (blue) calculated for the times between the blue dashed lines (17–24 ms) in (a) and (b) when the tearing mode amplitudes are at a minimum (high confinement period). A Maxwellian curve is fit to the spectrum (red).

magnetic tearing mode amplitudes, as illustrated in Fig. 8(b) by the m = 1, n = 5 (black), and n = 6 (red) mode amplitudes. High energy x-ray flux is observed to significantly increase during this time, indicating that the confinement of high energy electrons has improved. The PPCD period ends abruptly at 24.5 ms when the current density profile can no longer be sustained by inductive means. This results in a sawtooth crash which causes the plasma to become stochastic with the fast electrons diffusing out of the plasma core, as is indicated by the reduction of high energy x-ray flux. A spectrum (blue) calculated for the time period between the dashed blue lines in Fig. 8(c) shows the formation of a non-Maxwellian tail during PPCD, indicating a period of improved confinement and reduced transport. A Maxwellian curve (red) is fit to the spectrum for comparison. The measurements taken with the FXR detector during PPCD plasmas are consistent with measurements taken with the HXR detectors.[15]

The FXR detector provides high time resolution measurements in various MST plasma discharges. Improvements to the pulse height analysis software have led to more accurate and reliable photon pulse fits. The improved time resolution of the FXR detector system diminishes the system dead-time. This reduces the need to restrict the amount of x-ray flux reaching the detector, giving the system the versatility to be used in a variety of discharges with varying flux. Initial data in standard, QSH, and PPCD plasma discharges show the results are consistent with previous measurements made with SXR and HXR detectors. The improved time resolution of the diagnostic will allow future measurements to be made during time windows as small as 10 μs, a substantial improvement to the diagnostic suite. The capability of making measurements in small time windows will enable the dynamics of energetic electron generation and losses during sawtooth events and island growth in QSH plasmas to be uncovered and thoroughly studied.

ACKNOWLEDGMENTS

This material is based upon work supported by the U.S. Department of Energy Office of Science, Office of Fusion Energy Sciences program under Award No. DE-FC02-05ER54814 and the National Science Foundation under Grant No. PHY08-21899.

[1]K. V. Cone, J. Dunn, M. B. Schneider, H. A. Baldis, G. V. Brown, J. Emig, D. L. James, M. J. May, J. Park, R. Shepherd, and K. Widmann, Rev. Sci. Instrum. **81**, 10E318 (2010).
[2]K. L. Baker, R. E. Stewart, P. T. Steele, S. P. Vernon, and W. W. Hsing, Appl. Phys. Lett. **101**, 031107 (2012).
[3]H. Kawashima and T. Matoba, Rev. Sci. Instrum. **59**, 1816 (1988).
[4]B. Esposito, R. M. Solis, P. Van Belle, O. N. Jarvis, F. B. Marcus, G. Sadler, R. Sanchez, B. Fischer, P. Froissard, J. M. Adams, E. Cecil, and N. Watkins, Plasma Phys. Controlled Fusion **38**, 2035 (1996).
[5]P. V. Savrukhin, Rev. Sci. Instrum. **73**, 4243 (2002).
[6]J. Liptac, R. Parker, V. Tang, Y. Peysson, and J. Decker, Rev. Sci. Instrum. **77**, 103504 (2006).
[7]Y. P. Zhang, Y. Liu, J. W. Yang, X. Y. Song, M. Liao, X. Li, G. L. Yuan, Q. W. Yang, X. R. Duan, and C. H. Pan, Rev. Sci. Instrum. **80**, 126104 (2009).
[8]A. N. James, E. M. Hollmann, and G. R. Tynan, Rev. Sci. Instrum. **81**, 10E306 (2010).
[9]D. J. Clayton, A. F. Almagri, D. R. Burke, C. B. Forest, J. A. Goetz, M. C. Kaufman, and R. O'Connell, Rev. Sci. Instrum. **81**, 10E308 (2010).
[10]J. K. Lepson, P. Beiersdorfer, J. Clementson, M. Bitter, K. W. Hill, R. Kaita, C. H. Skinner, A. L. Roquemore, and G. Zimmer, Rev. Sci. Instrum. **83**, 10D520 (2012).
[11]S. Purohit, Y. S. Joisa, J. V. Raval, J. Ghosh, R. Tanna, B. K. Shukla, and S. B. Bhatt, Rev. Sci. Instrum. **85**, 11E419 (2014).
[12]D. W. Huang, Z. Y. Chen, Y. H. Luo, R. H. Tong, W. Yan, W. Jin, and G. Zhuang, Rev. Sci. Instrum. **85**, 11D845 (2014).
[13]R. N. Dexter, D. W. Kerst, T. W. Lovell, and S. C. Prager, Fusion Technol. **19**, 131 (1991).
[14]R. O'Connell, D. J. Den Hartog, C. B. Forest, and R. W. Harvey, Rev. Sci. Instrum. **74**, 2001 (2003).
[15]R. O'Connell, D. Hartog, C. Forest, J. Anderson, T. Biewer, B. Chapman, D. Craig, G. Fiksel, S. Prager, J. Sarff, S. Terry, and R. Harvey, Phys. Rev. Lett. **91**, 045002 (2003).
[16]D. J. Clayton, B. E. Chapman, R. O'Connell, A. F. Almagri, D. R. Burke, C. B. Forest, J. A. Goetz, M. C. Kaufman, F. Bonomo, P. Franz, M. Gobbin, and P. Piovesan, Phys. Plasmas **17**, 012505 (2010).
[17]S. C. Prager, A. F. Almagri, S. Assadi, J. A. Beckstead, R. N. Dexter, D. J. Den Hartog, G. Chartas, S. A. Hokin, T. W. Lovell, T. D. Rempel, J. S. Sarff, W. Shen, C. W. Spragins, and J. C. Sprott, Phys. Fluids B **2**, 1367 (1990).
[18]A. B. Rechester and M. N. Rosenbluth, Phys. Rev. Lett. **40**, 38 (1978).
[19]E. Scime, S. Hokin, N. Mattor, and C. Watts, Phys. Rev. Lett. **68**, 2165 (1992).
[20]R. M. Magee, D. J. Den Hartog, S. T. A. Kumar, A. F. Almagri, B. E. Chapman, G. Fiksel, V. V. Mirnov, E. D. Mezonlin, and J. B. Titus, Phys. Rev. Lett. **107**, 065005 (2011).
[21]S. Eilerman, J. K. Anderson, J. S. Sarff, C. B. Forest, J. A. Reusch, M. D. Nornberg, and J. Kim, Phys. Plasmas **22**, 020702 (2015).
[22]A. Baron, S. Kishimoto, J. Morse, and J. M. Rigal, J. Synchrotron Radiat. **13**, 131 (2006).
[23]J. R. Palmer and G. R. Morrison, Rev. Sci. Instrum. **63**, 828 (1992).
[24]S. Kishimoto, T. Mitsui, R. Haruki, Y. Yoda, T. Taniguchi, S. Shimazaki, M. Ikeno, M. Saito, and M. Tanaka, Rev. Sci. Instrum. **85**, 113102 (2014).
[25]P. Martin, L. Marrelli, G. Spizzo, P. Franz, P. Piovesan, I. Predebon, T. Bolzonella, S. Cappello, A. Cravotta, D. F. Escande, L. Frassinetti, S. Ortolani, R. Paccagnella, D. Terranova, B. E. Chapman, D. Craig, S. C. Prager, J. S. Sarff, P. Brunsell, J.-A. Malmberg, J. Drake, Y. Yagi, H. Koguchi, Y. Hirano, R. B. White, C. Sovinec, C. Xiao, R. A. Nebel, and D. D. Schnack, Nucl. Fusion **43**, 1855 (2003).
[26]L. Marrelli, P. Martin, G. Spizzo, P. Franz, B. E. Chapman, D. Craig, J. S. Sarff, T. M. Biewer, S. C. Prager, and J. C. Reardon, Phys. Plasmas **9**, 2868 (2002).
[27]J. S. Sarff, S. A. Hokin, H. Ji, S. C. Prager, and C. R. Sovinec, Phys. Rev. Lett. **72**, 3670 (1994).
[28]J. S. Sarff, A. F. Almagri, M. Cekic, C.-S. Chaing, D. Craig, D. J. Den Hartog, G. Fiksel, S. A. Hokin, R. W. Harvey, H. Ji, C. Litwin, S. C. Prager, D. Sinitsyn, C. R. Sovinec, J. C. Sprott, and E. Uchimoto, Phys. Plasmas **2**, 2440 (1995).